

Simultaneous rupture on conjugate faults during the 2018 Anchorage, Alaska, intraslab earthquake (MW 7.1) inverted from strong-motion waveforms

Yujia Guo (✉ guo@geor.or.jp)

Geo-Research Institute

Ken Miyakoshi

Geo-Research Institute

Masato Tsurugi

Geo-Research Institute

Full paper

Keywords: 2018 Anchorage earthquake, Intraslab earthquake, Subduction zone, Ground motion, Waveform inversion, Source rupture process, Conjugate fault, Source scaling relationship

Posted Date: November 16th, 2020

DOI: <https://doi.org/10.21203/rs.3.rs-42861/v3>

License:  This work is licensed under a Creative Commons Attribution 4.0 International License.

[Read Full License](#)

Version of Record: A version of this preprint was published on November 23rd, 2020. See the published version at <https://doi.org/10.1186/s40623-020-01315-x>.

1 **Simultaneous rupture on conjugate faults during the 2018 Anchorage, Alaska, intraslab**
2 **earthquake (M_w 7.1) inverted from strong-motion waveforms**

3

4 Author #1:

5 Yujia Guo

6 Geo-Research Institute, Kokumin-Kaikan Sumitomo-Seimei Bldg. 6F, 2-1-2 Otemae, Chuo-ku,

7 Osaka, Japan.

8 guo@geor.or.jp

9

10 Author #2:

11 Ken Miyakoshi

12 Geo-Research Institute, Kokumin-Kaikan Sumitomo-Seimei Bldg. 6F, 2-1-2 Otemae, Chuo-ku,

13 Osaka, Japan.

14 ken@geor.or.jp

15

16 Author #3:

17 Masato Tsurugi

18 Geo-Research Institute, Kokumin-Kaikan Sumitomo-Seimei Bldg. 6F, 2-1-2 Otemae, Chuo-ku,

19 Osaka, Japan.

20 tsurugi@geor.or.jp

21

22 **The corresponding author: #1**

23 **Abstract**

24 An M_w 7.1 ~50-km-deep intraslab earthquake within the Pacific/Yakutat slab underlying the
25 North American Plate struck Anchorage, southern Alaska, on November 30, 2018. The
26 ground-motion records very close to the source region of the Anchorage earthquake provide an
27 important opportunity to better understand the source characteristics of intraslab earthquakes in
28 this subduction zone. We estimated the kinematic rupture process during this earthquake using a
29 series of strong-motion waveform (0.05–0.4 Hz) inversions. Our inversions clearly indicate that
30 the Anchorage earthquake was a rare intraslab event with simultaneous rupture on two conjugate
31 faults, which are recognized sometimes for shallow crustal earthquakes but rarely for deep
32 intraslab earthquakes. Interestingly, one of the conjugate faults had low aftershock productivity.
33 This fault extends to great depth and may reflect a deep oceanic Moho or a local low-velocity
34 and high- V_P/V_S zone within the oceanic mantle. Even though the Anchorage earthquake was a
35 rare event due to the conjugate faults, we found that its kinematic source parameters such as the
36 slip amplitude and large-slip area nearly equal the global averages derived from source scaling
37 relationships for intraslab earthquakes. Because the source parameters comparable to the global
38 averages were also found for another large intraslab earthquake in the subducting Pacific/Yakutat
39 slab, these source parameters are likely an important source characteristic common to this
40 subduction zone.

41

42 **Keywords**

43 2018 Anchorage earthquake

44 Intraslab earthquake

45 Subduction zone

46 Ground motion
47 Waveform inversion
48 Source rupture process
49 Conjugate fault
50 Source scaling relationship

51

52 **Introduction**

53 At 17:29 Coordinated Universal Time (UTC) on November 30, 2018, an M_w 7.1 earthquake
54 occurred in southern Alaska ~20 km north of Anchorage at a depth of ~50 km (United States
55 Geological Survey (USGS) 2019; Figure 1). Under southern Alaska, the Yakutat terrane, which
56 has characteristics of an oceanic plateau (e.g., Christeson et al. 2010), and the Pacific Plate are
57 moving at the same slip rate but in slightly different directions with respect to the overlying
58 North American Plate (Elliott et al. 2010). The hypocenter of the 2018 Anchorage earthquake
59 was within the subducting Pacific or Yakutat slabs, the exact location of whose interface has not
60 yet been completely defined (e.g., Kim et al. 2014). This hypocenter was also located in the
61 upper part of the transition area from shallow-dipping to steep-dipping subduction (Hayes et al.
62 2018), and its focal mechanism indicates normal faulting (e.g., Ekström et al. 2012). Therefore,
63 there is no doubt that the Anchorage earthquake was an intraslab event.

64 Southern Alaska and Anchorage recently experienced two large intraslab earthquakes, the
65 1999 Kodiak Island (M_w 7.0; Hansen and Ratchkovski 2001) and 2016 Iniskin (M_w 7.1; Mann
66 and Abers 2020) earthquakes (Figure 1). Compared to these two events, the 2018 Anchorage
67 earthquake caused stronger ground motions resulting in structural damage to downtown
68 Anchorage because of its closer proximity to Anchorage (e.g., West et al. 2020). During the

69 Anchorage earthquake, the near-source seismograms were recorded by the stations of the United
70 States National Strong-Motion (NP) network and the Alaska Regional (AK) network. These
71 seismograms are very useful for investigating the source rupture of the earthquake. This study
72 estimates the kinematic source rupture process by performing waveform inversions of the
73 near-source strong-motion data at the frequency band of 0.05–0.4 Hz.

74 Kinematic rupture models of the Anchorage earthquake have already been derived from the
75 inversion of Liu et al. (2019) using geodetic, teleseismic, and strong-motion data and that of He
76 et al. (2020) using geodetic and teleseismic data. Their models indicate that a westward
77 steep-dipping fault rupture is preferred over an eastward shallow-dipping rupture. Even though
78 these studies focused on the rupture during the Anchorage mainshock, the fault geometries in
79 their rupture models insufficiently reproduce the spatially complex aftershock pattern (Figure 2),
80 as detailed later. Based on this pattern, Ruppert et al. (2020) and West et al. (2020) suggested the
81 possibility of a simultaneous rupture on two conjugate faults during the mainshock. The fault
82 geometry in our inversion considers this possibility and decreases the level of disagreement
83 between the mainshock fault geometry and the aftershock distribution.

84

85 **Conjugate fault geometry based on the relocated aftershock distribution**

86 We determined the fault planes in our inversion based on the mainshock and the aftershock
87 distributions relocated by the double-difference tomography algorithm (Ruppert et al. 2020). As
88 shown in Figure 2, the Anchorage mainshock was followed by a vigorous aftershock sequence
89 with ~1000 aftershocks ($M \geq 2$) within the three days following the mainshock. Because these
90 aftershocks exhibit no clear spatiotemporal migration (Figure S1) [see Additional file 1], the fault
91 planes assumed for the inversion should cover the entire range of these aftershocks. Most of the

92 aftershocks are concentrated north of the mainshock hypocenter at a depth range of 45–55 km.
93 Meanwhile, the mainshock hypocenter (149.9715° W, 61.3342° N) has a depth of 55.7 km. Even
94 though the relocated hypocenter depth of the mainshock is deeper than the depth of 46.7 km
95 estimated by USGS (2019), the depth of ~55 km better matches the arrival times of the observed
96 depth phases in the teleseismic waveforms (Liu et al. 2019). The relocated aftershocks form two
97 evident clusters: a southern cluster as marked by a dashed ellipse and a northern cluster as
98 marked by a dotted ellipse in Figure 2. The southern cluster dips eastward, and the northern
99 cluster dips westward (Figure 2b). In general, the aftershocks exhibiting a spatially complex
100 pattern reflect a mainshock rupture on two or more fault planes with different directions, which
101 results both in a difference between the moment tensor and first motion mechanisms and in a low
102 percentage of double-couple component in the moment tensor mechanism, as was the case in the
103 2008 northern Iwate, Japan, intraslab earthquake (e.g., Suzuki et al. 2009). However, for the
104 Anchorage mainshock, the difference between the moment tensor and first motion mechanisms is
105 very small and the percentage of double-couple component is significantly high, ~90% (USGS
106 2019). These facts suggest a possibility that the Anchorage mainshock was an event with two
107 conjugate faults corresponding to the two aftershock clusters. The two aftershock clusters, which
108 share a similar focal mechanism (Ruppert et al. 2020), also stimulate us to explore this possibility.
109 Meanwhile, there is an alternative possibility where the mainshock occurred on only one of the
110 conjugate faults and then induced the aftershocks to occur along the other of the conjugate faults.
111 Therefore, as explained later, the inversion of the present study considered several possible
112 cases.

113 Based on the cross-sectional view perpendicular to the strike angle (5°) of the moment tensor
114 solution (Figure 2b), we found that the southern and northern clusters dip with angles of $\sim 30^\circ$

115 and $\sim 60^\circ$, respectively. These dip angles are consistent with those of the two nodal planes in the
116 focal mechanisms for the mainshock and aftershocks (Ruppert et al. 2020). The mainshock
117 hypocenter is likely on the plane of the southern cluster rather than on that of the northern cluster.
118 We also checked another cross-sectional view (Figure S2) [see Additional file 1], which was
119 perpendicular to the apparent strike angle (340°) of the southern cluster in the map view (Figure
120 2a), and confirmed that the dip angles in this direction had large gaps relative to those of the two
121 nodal planes in the focal mechanisms for the aftershocks. Based on the directional superiority of
122 Figure 2 over Figure S2, our inversion for the Anchorage mainshock assumed two fault planes,
123 one with a strike of 5° and a dip of 30° and the other with a strike of 185° and a dip of 60°
124 (Figure 3). These strikes and dips agree well with those of the Global Centroid Moment Tensor
125 (GCMT; Ekström et al. 2012) solution (strike = 7° , 189° ; dip = 26° , 64°). As explained later,
126 these planes were divided into three segments (S1, S2, and S3) for our inversion strategy.
127 Segments S1 and S2 represent the deep and shallow portions of the eastward shallow-dipping
128 fault, respectively, and segment S3 represents the westward steep-dipping fault. For simplicity,
129 we assumed an identical fault length of 34 km for these segments. The fault width of segment S1
130 is 18 km, and segments S2 and S3 have fault widths of 16 km. The hypocenter is located on
131 segment S1. We ruled out the possibility of the hypocenter being located at the intersection of the
132 three segments because the shortest distance from the hypocenter to the intersection (3 km) is
133 greater than the relocation error (<0.5 km) in Ruppert et al. (2020). The rigidity of the fault
134 planes was assumed to be 56 GPa (Eberhart-Phillips et al. 2006, 2019) without a depth
135 dependence.

136

137 **Observed data**

138 Our inversion selected nine strong-motion stations (Figure 4): seven AK network stations and
139 two NP network stations. The station distribution provides good azimuthal coverage except
140 southwest of the source region. Even though there is a southwestern station (Figure 4) located
141 above the thickest sediments of the Cook Inlet sedimentary basin (Shellenbaum et al. 2010;
142 Silwal et al. 2018; Figure 1), we excluded this station because strong 3D basin effects (e.g.,
143 Mann and Abers 2020; Smith and Tape, 2020) complicate the phases of seismic waves, enhance
144 the amplitudes even at extremely low frequency (~ 0.1 Hz), and therefore can adversely affect our
145 inversion results. We confirmed that nine stations were sufficient to ensure a good spatial
146 resolution of our inversion, even though the station coverage on the western side of the source
147 region was slightly poorer than that on the eastern side. The observed three-component
148 acceleration waveforms were integrated to velocity waveforms, band-pass filtered between 0.05
149 Hz and 0.4 Hz, and resampled with a sampling frequency of 5 Hz. The upper limit of 0.4 Hz was
150 determined to ensure the accuracy of the Green’s functions in our inversion. The waveforms
151 lasting 20–30 s from the manually picked *P*-wave onsets were used as the inversion data.

152

153 **Inversion method**

154 We used a multi-time-window linear waveform-inversion method (Hartzell and Heaton 1983),
155 where the rupture process was spatially discretized by dividing the source faults into subfaults (*if*
156 = 1, *nf*) and temporally discretized on each subfault by representing the slip histories in two
157 orthogonal slip directions (*ir* = 1, 2) with multiple time windows (*it* = 1, *nt*). A synthetic
158 waveform $U^{\text{syn}}(t)$ is modeled as follows:

$$U^{\text{syn}}(t) = \sum_{if}^{nf} \sum_{it}^{nt} \sum_{ir}^2 m_{if,it,ir} \Omega \left[t - \Delta t(it - 1) - \frac{\xi_{if}}{V_R} \right] * G_{if,ir}(t), \quad (1)$$

159 where $\Omega(t)$ is a basis function representing a time window; Δt , the time interval between

160 consecutive time windows; ξ_{if} , the distance from the hypocenter; V_R , the rupture velocity
161 triggering the first time window; and $G_{if,ir}(t)$, the Green's function. The model parameters of
162 the waveform inversion were slip amplitudes in the two slip directions for each time window of
163 each subfault ($m_{if,it,ir}$). All three fault segments in our inversion, S1, S2, and S3, were divided
164 into 2 km \times 2 km subfaults. Three time windows, each of which was a smoothed ramp function
165 with a duration of 2 s separated from each other by 1 s were used on each subfault. These time
166 windows permit a maximum slip duration of 4 s and are enough to represent the total rupture on
167 each subfault. These model parameters were obtained by limiting the rake angle (slip direction)
168 to be within $\pm 45^\circ$ centered at 270° (pure normal faulting) and solving a non-negative
169 least-squares problem (Lawson and Hanson 1974). For the inversion stability, a spatiotemporal
170 smoothing constraint (e.g., Sekiguchi et al. 2000) was also imposed on the model parameters for
171 each time window:

$$\mathbf{S} \equiv \left(\frac{\partial^2}{\partial x^2} + \frac{\partial^2}{\partial y^2} \right) \mathbf{m} = \mathbf{0}, \quad (2)$$

172 where x and y represent the along-strike and along-dip directions, respectively; and \mathbf{m} is the
173 model vector. Therefore, the observation equation is given as

$$\begin{pmatrix} \mathbf{G} \\ \lambda \mathbf{S} \end{pmatrix} \mathbf{m} = \begin{pmatrix} \mathbf{d} \\ \mathbf{0} \end{pmatrix}, \quad (3)$$

174 where \mathbf{G} and \mathbf{d} are the matrices comprising the Green's functions and data vector, respectively.
175 The appropriate weight (λ) of the smoothing constraint was selected by referring to the Akaike
176 Bayesian information criterion (ABIC; Akaike 1980; Figure S3a [see Additional file 1]). The
177 constant V_R on each subfault was determined based on the best value of the variance reduction
178 (Figure S3b) [see Additional file 1], which measures the degree of the fit between the observed
179 and synthetic data:

$$\text{variance reduction} = 1 - \frac{\sum_{j=1}^N \sum_{i=1}^3 \sum_{t=1}^T \left(U_{ij}^{\text{obs}}(t) - U_{ij}^{\text{syn}}(t) \right)^2}{\sum_{j=1}^N \sum_{i=1}^3 \sum_{t=1}^T \left(U_{ij}^{\text{obs}}(t) \right)^2}, \quad (4)$$

180 where N , 3, and T are the numbers of stations, waveform components, and time steps,
 181 respectively; and $U^{\text{obs}}(t)$ represent the observed waveform.

182 We assumed 1D layered velocity structure models and calculated the Green's functions for
 183 each subfault using the discrete wavenumber method (Bouchon 1981) and the
 184 reflection/transmission coefficient matrix method (Kennett and Kerry 1979). For each station, the
 185 1D layered model was extracted from the 3D gridded velocity structure model of
 186 Eberhart-Phillips et al. (2006, 2019). The layered model in the present study was constructed by
 187 substituting the physical parameters of the non-grid point with those of the grid point closest to it.
 188 Because their 3D model primarily imaged deep structures such as the crust and mantle and
 189 therefore did not sufficiently include near-surface low-velocity structures such as sedimentary
 190 basins, which amplify and complicate the observed low-frequency (<1-Hz) waveforms (e.g.,
 191 Boore 2004; Moschetti et al. 2020), we replaced the shallowest portion of the model of
 192 Eberhart-Phillips et al. (2006, 2019) with four layers with S -wave velocities of 0.40–2.25 km/s
 193 referring to Dutta et al. (2007). We determined the thicknesses of these four layers via trial and
 194 error such that the phases and amplitudes in the synthetic waveforms (0.1–0.4 Hz) for two
 195 moderate-sized aftershocks (M_w 5.0 at 7:57 UTC and M_w 4.5 at 12:44 UTC on December 1,
 196 2018; Figure 2 and Table S1 [see Additional file 1]) satisfactorily reproduced the observations
 197 (Figure S4) [see Additional file 1]. Double-couple point sources with smoothed ramp functions
 198 and focal information based on Ekström et al. (2012) and Ruppert et al. (2020) were assumed to
 199 calculate the synthetic waveforms. Q values based on the formula of Brocher (2008) were used
 200 for the calculations. The calibrated 1D velocity structure models (Figure 4 and Table S2 [see
 201 Additional file 1]) show thick low-velocity layers relative to the initial model (Eberhart-Phillips

202 *et al.* 2006, 2019) for the stations AHOU, AWCH, and SKN, located inside the sedimentary
203 basins and away from the basin edges.

204 To verify if a simultaneous rupture on two conjugate faults occurred during the Anchorage
205 mainshock, we performed waveform inversions for three cases (Figure 3). Case A assumes a
206 rupture on a single, eastward shallow-dipping fault (segments S1 and S2), which is similar to the
207 eastward dipping fault model in the supporting information of Liu *et al.* (2019). Meanwhile,
208 cases B and C assume a conjugate rupture both on the eastward shallow-dipping and westward
209 steep-dipping faults (segment S3). The difference between the two cases is the absence (case B)
210 or presence (case C) of the shallow portion of the eastward shallow-dipping fault (segment S2).
211 In cases B and C, we assume that the rupture on segment S3 radiated without a time delay from
212 the intersection point (the black star in Figure 3), with the rupture propagating on segment S1
213 arriving first. As mentioned earlier, the intersection point should not be the same as the
214 hypocenter, else segment S3 will not agree with the location of the northern aftershock cluster.
215 We also assumed that the slip between the westward steep-dipping (segment S3) and eastward
216 shallow-dipping (segments S1 and S2) faults could be discontinuous. These assumptions follow
217 the inversions of earthquakes with multiple fault planes (e.g., Suzuki *et al.* 2009).

218 Segments S2 and S3 and the up-dip portion of segment S1 were assumed based on the
219 aftershock distribution. Meanwhile, in all three cases, the down-dip extension of segment S1
220 (Figure 3), which resulted in a significantly larger depth relative to the aftershock clusters, was
221 determined via a preliminary inversion trial. Figure 5 shows that, if segment S1 has a small fault
222 width (6 km) that does not extend into the eastern zone with low aftershock activity, an
223 extremely large slip is estimated at its eastern edge. This means that segment S1 should be
224 further expanded. We tested several fault widths of segment S1 (Figure S5) [see Additional file

225 1] and determined its width to be 18 km, as mentioned earlier.

226

227 **Inversion results for the three cases**

228 Table 1 summarizes our inversion results, Figures 6 (cases A, B, and C), 7a (case A), 8a (case
229 B), and 9a (case C) show the final slip distributions, and Figures 7b (case A), 8b (case B), and 9b
230 (case C) show the distributions of the maximum slip velocities and moment rate functions. The
231 optimal rupture velocities triggering the first time windows for all three cases were determined to
232 be 2.9 km/s (Figure S3b), which corresponded to 69% of the average *S*-wave velocity around the
233 source faults. The total seismic moments are 1.2–1.4 times as large as that of the GCMT solution
234 (4.8×10^{19} Nm). The seismic moment on segment S1 accounts for 61%, 59%, and 44% of the
235 total seismic moment for cases A, B, and C, respectively. The seismic moment of only segment
236 S2 and/or S3 is significantly smaller than that of the GCMT solution. Even though segment S1
237 had low aftershock activity that led us to debate whether the mainshock rupture extended to it,
238 the large percentage of segment S1 suggests that it ruptured during the mainshock. Furthermore,
239 if segment S1 had small fault width shown in Figure 5, the observed waveforms at the eastern
240 stations away from the source region could not be reasonably reproduced (Figure S5b).

241 The spatial distributions of the estimated large slips and aftershocks are complementary to
242 each other (Figure 6). On segments S1 and S2 (cases A and C), large slips occur east (~60 km in
243 depth) and north (~50 km in depth) of the hypocenter, even though the northern slip in case C is
244 slightly uncertain. These large slips surround most of the southern aftershock cluster. On segment
245 S3 (cases B and C), the large slip is located at a depth of ~50 km just south of the densest
246 clustering of northern aftershocks. We can directly compare the slip distribution of case A with
247 that of the eastward shallow-dipping model in Liu et al. (2019) because the two have similar

248 fault geometries. The slip distribution of case A is consistent with that of Liu et al. (2019) in that
249 the large slips are located a small distance from the hypocenter.

250 In case B, the peak values of the large slips on the conjugate segments S1 and S3 are
251 comparable (Figures 6 and 8a). In case C, the added segment S2 results in a slip separation from
252 S3 to S2 and therefore in a reduction of the large slip on S3. The spatial slip patterns on segments
253 S2 and S3 in case C are similar to those in cases A and B, respectively. In case C, even though
254 the large slip on segment S3 is reduced, its peak value is still ~ 1.5 times greater than the
255 maximum slip on segment S2 (Figures 6 and 9a).

256

257 **Determination of the preferable case**

258 Cases A and B have comparable total variance reductions (Table 1). However, we favor case B,
259 that is, the westward steep-dipping fault in the upper half of the source (segment S3), based on
260 its better reproduction of the observed main pulses at station AHOU, which lies adjacent to the
261 northern edge of the source fault and recorded considerable amplitudes. Two large pulses can be
262 seen at a lapse time of 10–15 s in the east–west component (Figure 10b). Segment S3 in case B
263 reproduces the amplitudes of both pulses reasonably well, even though segment S2 in case A
264 reproduces only the second pulse. This is primarily due to the upward rupture propagation on the
265 steep-dipping segment S3. To confirm that case B was better than case A, we used two virtual
266 line source models and performed a numerical test (Figure 11). The rupture on line source
267 models A and B propagated toward the farthest point on segments S2 and S3, respectively. Note
268 that in this numerical test, segment S1 was not considered because it is a segment common to
269 inversion cases A and B. For calculating the synthetic waveforms, we assumed a unit slip, pure
270 normal faulting, and a rupture velocity of 2.9 km/s. The spatial pattern of the synthetic peak

271 amplitudes for line source A, where the peak amplitude for the station on the western side of the
272 hypocenter (SSN) was larger than that for the stations on the eastern side and above the thick
273 sediments (AHOU and AWCH; Figure 4), cannot be found in the observation. This fact suggests
274 that it is likely that the main rupture did not extend into segment S2 in inversion case A. On the
275 other hand, the synthetic spatial pattern for line source B, which includes the northeastward
276 rupture propagation on the steep-dipping segment S3, is similar to the observation. Analyses of
277 interferometric synthetic aperture radar images (e.g., He et al. 2020; West et al. 2020) also
278 indicate that the westward steep-dipping fault is required to explain the significant uplift on the
279 eastern side of the source region.

280 Together with the comparison between cases A and B (Figures 10b and 11), the comparison
281 between cases B and C also eliminates the possibility of the mainshock rupture on segment S2.
282 Table 1 shows that the variance reduction of case C is significantly higher than that of case B,
283 which means that the total waveform fit (Figure 10) is improved by the addition of segment S2.
284 However, this improvement is not surprising because the added segment S2 increases the number
285 of model parameters and therefore allows a more detailed waveform fit. In general, a model with
286 more degrees of freedom and a higher variance reduction is not always better in that it may not
287 correspond to other datasets. To judge whether case B or C is better, we calculated the values of
288 the Akaike information criterion (AIC; Akaike 1974), which considers both the data fit and the
289 model complexity/simplicity and is often used for model selection. We found that case B ($2.0 \times$
290 10^2) has a smaller AIC value than case C (9.7×10^2). Therefore, we suggest that case B is the
291 better model and that most of the actual rupture during the Anchorage mainshock was restricted
292 to segments S1 and S3 and did not extend to segment S2. Even though the complex aftershock
293 distribution and the large focal depth made it difficult to precisely determine the extent of the

294 source faults during the Anchorage mainshock, the above comparisons lead us to conclude that
295 case B is the most plausible of the three cases.

296

297 **Discussion on the source characteristics of case B**

298 Here, we detail the source characteristics of case B, our best model. Because large slips have a
299 major influence on ground motions, an understanding of the characteristics of the large slips
300 during the Anchorage earthquake will contribute to ground-motion predictions of future intraslab
301 earthquakes. To identify the large slip area in case B, we used the criteria proposed by Somerville
302 et al. (1999) as follows. First, we decided that the rupture area for case B was the same as the
303 combined area of the modeled segments S1 and S3 because the average slips on the fault-edge
304 rows/columns for case B (Figure 8a) were greater than 0.3 times the average slips over the
305 modeled segments. Then, we defined the rectangular area of the subfaults with ≥ 1.5 times the
306 average slip of the rupture area as a large slip area (called “asperity area” in Somerville et al.
307 (1999)). As a result, we obtained two large slip areas in case B. One (A1) is on the down-dip side
308 of the hypocenter on segment S1, and the other (A2) is in the central portion of segment S3
309 (Figure 8). A1 and A2 were generated 2.5–5 s and 5–10 s after the rupture initiation, respectively
310 (Figure 12a). As illustrated in the contributions of A1 and A2 to the velocity waveforms at three
311 near-source stations (Figure 12b), much of the amplitude can be explained by these large slip
312 areas and the contribution of A2 occurs subsequent to that of A1. The synthetic peak amplitudes
313 are produced by A2, and its value at the northern station AHOU is the largest due to the forward
314 directivity resulting from the upward and northward rupture propagation of A2. At stations
315 AHOU and K209, A2 yields larger amplitudes than A1 because of the forward directivity and the
316 shallower depth of A2, respectively. Meanwhile, the amplitude from A1 is comparable to that

317 from A2 at the eastern station K217 because of the eastward rupture propagation of A1. The two
318 large slip areas have a total dimension that is 17% of the rupture area. This percentage is
319 equivalent to that calculated by Iwata and Asano (2011), who proposed scaling relationships of
320 the source parameters for M 7–8-class intraslab earthquakes. Even though several global source
321 scaling relationships for intraslab earthquakes have been published (e.g., Iwata and Asano 2011;
322 Allen and Hayes 2017), these relationships were developed using no source parameter data from
323 southern Alaskan (i.e., Alaska–Aleutian) earthquakes because of the low intraslab activity in this
324 area compared to other subduction zones. In comparison with Iwata and Asano (2011), we found
325 that the large slip areas of the Anchorage earthquake had a globally average total dimension
326 (Figure 13a).

327 The total dimension and average slip of the rupture area are also key parameters for
328 constructing source models of scenario earthquakes. We compared these parameters of the
329 Anchorage earthquake to source scaling relationships (Iwata and Asano 2011; Allen and Hayes
330 2017). Such scaling relationships can also account for the dimension (Figure 13b) and average
331 slip (Figure 13c) of the rupture area of the Anchorage earthquake, as well as the dimension of the
332 large slip area. Figure 13 also compares the Anchorage earthquake to the 2016 Iniskin earthquake
333 (USGS 2018) in southern Alaska, the source parameters (Figure S6) [see Additional file 1] of
334 which were also obtained using the criteria of Somerville et al. (1999). The previously described
335 feature is shared by the Iniskin earthquake. Even though source parameters include regional
336 perturbations associated with differences in the subduction environment (e.g., Stirling et al.
337 2013), we suggest that the source parameters of intraslab earthquakes in southern Alaska nearly
338 equal the global average source parameters.

339 During the Anchorage earthquake, the large slip area A2 propagated in the direction away

340 from downtown Anchorage (Figure 12). Despite the source parameters comparable to the global
341 averages and the backward direction, ground motions were observed with large low-frequency
342 amplitudes (e.g., Moschetti et al. 2020). Figure 14 shows the velocity Fourier spectra at several
343 stations in downtown Anchorage. The eastern stations (ALUK and K215), which are located near
344 the edge of the Cook Inlet Basin, have no clear spectral peaks in the low frequency. This means
345 that the observed large low-frequency ground-motions did not originate from the earthquake
346 source. Meanwhile, the western stations farther from the basin edge (8036 and K220) have
347 remarkably large amplitude levels at <0.5 Hz and spectral peaks at 0.2–0.3 Hz. The spectral
348 difference between the eastern and western stations suggests that the large low-frequency
349 ground-motions in downtown Anchorage were primarily due to site amplification effects
350 associated with the basin, rather than source effects.

351

352 **Tectonic structure around the source region**

353 The oceanic crust is generally characterized by a low-velocity and high- V_P/V_S zone. Because
354 this zone suggests the existence of the fluid released by dehydration reactions, which reduces the
355 effective normal stress and fault strength, intraslab earthquakes usually occur within this zone
356 (e.g., Raleigh and Paterson, 1965). Around the source region of the Anchorage earthquake, a
357 laterally extended zone with low-velocity and high- V_P/V_S (>1.8) was detected at a depth of ~ 50
358 km (e.g., Eberhart-Phillips et al. 2006, 2019; Kim et al. 2014; Table S2). This means that the
359 oceanic Moho of the subducting Pacific/Yakutat slab extends to at least ~ 50 km. As shown in
360 Figure 3, the lower limit of our conjugate fault model penetrated to a greater depth of 63 km.
361 Note that, due to the eastward shallow-dipping fault (segment S1), this depth was shallower than
362 the ~ 70 km found by Liu et al. (2019) and He et al. (2020), whose best models were on a single,

363 westward steep-dipping fault. Our conjugate fault model suggests two possibilities. The first is
364 that the oceanic Moho has a depth of 60–65 km at the edge of the shallow-dipping
365 Pacific/Yakutat slab. If this is true, the total thickness of the oceanic crust from the slab surface
366 (30–35 km) is ~30 km. The second possibility is that, even though the oceanic Moho is located at
367 ~50 km, there is a local low-velocity and high- V_P/V_S zone within the oceanic mantle (e.g.,
368 Nakajima et al. 2011) around the source region of the Anchorage earthquake. To distinguish
369 between these possibilities, it is important to conduct further investigations of seismic structure
370 imaging with finer resolution.

371

372 **Conclusions**

373 We performed strong-motion waveform (0.05–0.4 Hz) inversions and proposed a kinematic
374 rupture model of the 2018 Anchorage intraslab earthquake (M_w 7.1) based on the aftershock
375 distribution as relocated by Ruppert et al. (2020). Our inversions revealed a simultaneous rupture
376 on two conjugate faults, an eastward shallow-dipping fault and a westward steep-dipping fault.
377 The preferred rupture model suggests that the shallower side of the eastward shallow-dipping
378 fault, where aftershocks formed a distinct cluster, experienced little rupture during the mainshock.
379 Our conjugate faults also showed the possibility of a deep oceanic Moho or a local low-velocity
380 and high- V_P/V_S zone within the oceanic mantle of the subducting Pacific/Yakutat slab. On each
381 of the conjugate faults, we identified one large slip area that significantly contributed to the
382 observed ground motions. Unlike shallow crustal earthquakes, there have been few identified
383 large intraslab earthquakes with conjugate faults. We found that, even though the Anchorage
384 earthquake was a rare intraslab event in terms of having conjugate faults, its source parameters,
385 such as its slip amplitude and fault dimension, are consistent with the averages of global intraslab

386 earthquakes.

387

388

389 **Supplementary information**

390 Additional file 1: This is a pdf file and consists of Tables S1–S2 and Figures S1–S6.

391

392 **List of abbreviations**

393 ABIC: Akaike Bayesian information criterion

394 AIC: Akaike information criterion

395 AK: Alaska Regional

396 AVO: Alaska Volcano Observatory

397 GCMT: Global Centroid Moment Tensor

398 NP: United States National Strong-Motion

399 USGS: United States Geological Survey

400 UTC: Coordinated Universal Time

401

402 **Availability of data and materials**

403 The strong motion data recorded at the AK and NP Network stations were obtained from the

404 Incorporated Research Institutions for Seismology Data Management Center at

405 http://ds.iris.edu/wilber3/find_event.

406

407 **Competing interests**

408 The authors declare that they have no competing interests

409

410 **Funding**

411 This work is funded by the 2019 research project “the methodology of ground motion prediction
412 for megathrust earthquakes” by the Nuclear Regulation Authority, Japan.

413

414 **Authors' contributions**

415 YG performed waveform inversions, interpretation and manuscript preparation. KM and MT
416 provided supervision of work and manuscript evaluation. All authors read and approved the final
417 manuscript.

418

419 **Acknowledgements**

420 Figures are drawn using the Generic Mapping Tools version 4.5.2
421 (<http://www.soest.hawaii.edu/gmt/>; Wessel and Smith 1998). We thank Kimiyuki Asano and two
422 anonymous reviewers for their helpful comments.

423

424 **Ethics approval and consent to participate**

425 Not applicable.

426

427 **Consent for publication**

428 Not applicable.

429

430

431 **References**

432 Akaike H (1974) A new look at the statistical model identification. *IEEE Trans Automat Contr*
433 19:716–723. doi:10.1109/TAC.1974.1100705

434 Akaike H (1980) Likelihood and the Bayes procedure. *Trabajos de Estadística Y de Investigación*
435 *Operativa* 31:143–166. doi:10.1007/BF02888350

436 Allen TI, Hayes GP (2017) Alternative rupture-scaling relationships for subduction interface and
437 other offshore environments. *Bull Seismol Soc Am* 107:1240–1253. doi:
438 10.1785/0120160255

439 AVO (2016) Latitudes and longitudes of Alaskan volcanoes.
440 <https://www.avo.alaska.edu/volcanoes/latlong.php>. Accessed June 2020

441 Boore DM (2004) Ground motion in Anchorage, Alaska, from the 2002 Denali fault earthquake:
442 Site response and displacement pulses. *Bull Seismol Soc Am* 94:S72–S84. doi:
443 10.1785/0120040606

444 Bouchon M (1981) A simple method to calculate Green's functions for elastic layered media.
445 *Bull Seismol Soc Am* 71:959–971

446 Brocher TM (2008) Key elements of regional seismic velocity models for long period ground
447 motion simulations. *J Seismol* 12:217–221. doi:10.1007/s10950-007-9061-3

448 Christeson GL, Gulick SPS, van Avendonk HJA, Worthington LL, Reece RS, Pavlis TL (2010)
449 The Yakutat terrane: Dramatic change in crustal thickness across the Transition fault, Alaska.
450 *Geology* 38:895–898. doi:10.1130/G31170.1

451 Dutta U, Satoh T, Kawase H, Sato T, Biswas N, Martirosyan A, Dravinski M. (2007) *S*-wave
452 velocity structure of sediments in Anchorage, Alaska, estimated with array measurements of
453 microtremors. *Bull Seismol Soc Am* 97:234–255. doi:10.1785/0120060001

454 Eberhart-Phillips D, Christensen DH, Brocher TM, Hansen R, Ruppert NA, Haeussler PJ, Abers

455 GA (2006) Imaging the transition from Aleutian subduction to Yakutat collision in central
456 Alaska, with local earthquakes and active source data. *J Geophys Res* 111:B11303.
457 doi:10.1029/2005JB004240

458 Eberhart-Phillips D, Nayak A, Ruppert N, Thurber C (2019) Alaska 2018 update for
459 USGSG18AP00017: Initial development of Alaska Community Seismic Velocity Models
460 (Version AKEP2018) [Data set]. Zenodo. doi:10.5281/zenodo.2544925

461 Ekström G, Nettles M, Dziewonski AM (2012) The global CMT project 2004–2010:
462 Centroid-moment tensors for 13,017 earthquakes. *Phys Earth Planet Inter* 200–201:1–9.
463 doi:10.1016/j.pepi.2012.04.002

464 Elliott JL, Larsen CF, Freymueller JT, Motyka RJ (2010) Tectonic block motion and glacial
465 isostatic adjustment in southeast Alaska and adjacent Canada constrained by GPS
466 measurements. *J Geophys Res* 115:B09407. doi:10.1029/2009JB007139

467 Hansen RA, Ratchkovski NA (2001) The Kodiak Island, Alaska M_w 7 earthquake of 6 December
468 1999. *Seismol Res Lett* 72:22–32. doi:10.1785/gssrl.72.1.22

469 Hartzell SH, Heaton TH (1983) Inversion of strong ground motion and teleseismic waveform
470 data for the fault rupture history of the 1979 Imperial Valley, California, earthquake. *Bull*
471 *Seismol Soc Am* 73:1553–1583

472 Hayes GP, Moore GL, Portner DE, Hearne M, Flamme H, Furtney M, Smoczyk GM (2018)
473 Slab2, a comprehensive subduction zone geometry model. *Science* 362:58–61.
474 doi:10.1126/science.aat4723

475 He P, Wen Y, Chen Y, Xu C, Ding K (2020) Coseismic rupture geometry and slip rupture process
476 during the 2018 M_w 7.1 Anchorage, south-central Alaska earthquake: Intraplate normal
477 faulting by slab tear constrained by geodetic and teleseismic data. *Earth Space Sci*

478 7:e2019EA000924. doi:10.1029/2019EA000924

479 Iwata T, Asano K (2011) Characterization of the heterogeneous source model of intraslab
480 earthquakes toward strong ground motion prediction. *Pure Appl Geophys* 168:117–124.
481 doi:10.1007/s00024-010-0128-7

482 Kennett BLN, Kerry NJ (1979) Seismic waves in a stratified half space. *Geophys J Int* 57:557–
483 583. doi:10.1111/j.1365-246X.1979.tb06779.x

484 Kim Y, Abers GA, Li J, Christensen D, Calkins J, Rondenay S (2014) Alaska Megathrust 2:
485 Imaging the megathrust zone and Yakutat/Pacific plate interface in the Alaska subduction
486 zone. *J Geophys Res Solid Earth* 119:1924–1941. doi:10.1002/2013JB010581

487 Lawson CL, Hanson RJ (1974) Solving least squares problems. Prentice Hall, New Jersey

488 Liu C, Lay T, Xie Z, Xiong X (2019) Intraslab deformation in the 30 November 2018 Anchorage,
489 Alaska, *M_w* 7.1 earthquake. *Geophys Res Lett* 46:2449–2457. doi:10.1029/2019GL082041

490 Mann ME, Abers GA (2020) First-order mantle subduction-zone structure effects on ground
491 motion: The 2016 *M_w* 7.1 Iniskin and 2018 *M_w* 7.1 Anchorage earthquakes. *Seismol Res*
492 *Lett* 91:85–93. doi:10.1785/0220190197

493 Moschetti MP, Thompson EM, Rekoske J, Hearne MG, Powers PM, McNamara DE, Tape C
494 (2020) Ground-motion amplification in Cook Inlet region, Alaska, from intermediate-depth
495 earthquakes, including the 2018 *M_w* 7.1 Anchorage earthquake. *Seismol Res Lett* 91:142–
496 152. doi:10.1785/0220190179

497 Nakajima J, Hasegawa A, Kita S (2011) Seismic evidence for reactivation of a buried hydrated
498 fault in the Pacific slab by the 2011 *M_w* 9.0 Tohoku earthquake. *Geophys Res Lett* 38:L00G06.
499 doi:10.1029/2011GL048432

500 Raleigh CB, Paterson MS (1965) Experimental deformation of serpentinite and its tectonic

501 implications. *J Geophys Res* 70:3965–3985. doi:10.1029/JZ070i016p03965

502 Ruppert NA, Nayak A, Thurber C, Richards C (2020) Aftershock Analysis of the 2018 *M*_w 7.1
503 Anchorage, Alaska, earthquake: Relocations and regional moment tensors. *Seismol Res Lett*
504 91:114–125. doi:10.1785/0220190199

505 Sekiguchi H, Irikura K, Iwata T (2000) Fault geometry at the rupture termination of the 1995
506 Hyogo-ken Nanbu earthquake. *Bull Seismol Soc Am* 90:117–133. doi:10.1785/0119990027

507 Shellenbaum DP, Gregersen LS, Delaney PR (2010) Top Mesozoic unconformity depth map of
508 the Cook Inlet basin, Alaska: Report of investigation 2010–2. Alaska Division of Geological
509 & Geophysical Surveys. doi:10.14509/21961

510 Silwal V, Tape C, Lomax A (2018) Crustal earthquakes in the Cook Inlet and Susitna region of
511 southern Alaska. *Tectonophysics* 745:245–263. doi:10.1016/j.tecto.2018.08.013

512 Smith K, Tape C (2020) Seismic response of Cook Inlet sedimentary basin, Southern Alaska.
513 *Seismol Res Lett* 91:33–55. doi:10.1785/0220190205

514 Somerville P, Irikura K, Graves R, Sawada S, Wald D, Abrahamson N, Iwasaki Y, Kagawa T,
515 Smith N, Kowada A (1999) Characterizing crustal earthquake slip models for the prediction
516 of strong ground motion. *Seismol Res Lett* 70:59–80. doi:10.1785/gssrl.70.1.59

517 Stirling M, Goned T, Berryman K, Litchfield N (2013) Selection of earthquake scaling
518 relationships for seismic-hazard analysis. *Bull Seismol Soc Am* 103:2993–3011.
519 doi:10.1785/0120130052

520 Suzuki W, Aoi S, Sekiguchi H (2009) Rupture process of the 2008 northern Iwate intraslab
521 earthquake derived from strong-motion records. *Bull Seismol Soc Am* 99:2825–2835.
522 doi:10.1785/0120080331

523 USGS (2018) *M* 7.1 - 86km E of Old Iliamna, Alaska.

524 <https://earthquake.usgs.gov/earthquakes/eventpage/ak01613v15nv/executive>. Accessed June
525 2020

526 USGS (2019) *M* 7.1 - 14km NNW of Anchorage, Alaska.
527 <https://earthquake.usgs.gov/earthquakes/eventpage/ak018fcnsk91/executive>. Accessed June
528 2020

529 Wessel P, Smith WHF (1998) New, improved version of Generic Mapping Tools released. *Eos*
530 *Trans AGU* 79:579. doi:10.1029/98EO00426

531 West ME, Bender A, Gardine M, Gardine L, Gately K, Haeussler P, Hassan W, Meyer F,
532 Richards C, Ruppert NA, Tape C, Thornley J, Witter RC (2020) The 30 November 2018 *M_w*
533 7.1 Anchorage earthquake. *Seismol Res Lett* 91:66–84. doi:10.1785/0220190176

534 Table 1

535 Parameters of the Three Inversion Cases.

	Case A	Case B	Case C
Segments	S1, S2	S1, S3	S1, S2, S3
Seismic moment	6.6×10^{19} Nm (M_w 7.1)	5.9×10^{19} Nm (M_w 7.1)	6.8×10^{19} Nm (M_w 7.2)
Average slip			
All segments	1.1 m	0.96 m	0.75 m
Segment S1 and/or S2 (eastward shallow-dipping)	1.1 m	1.1 m	0.80 m
Segment S3 (westward steep-dipping)	-	0.84 m	0.65 m
Rupture velocity	2.9 km/s	2.9 km/s	2.9 km/s
Variance reduction	0.65	0.65	0.73

536

537 **Figure 1** Map of southern Alaska.

538 Stars mark the epicenters of the Anchorage, Kodiak Island, and Iniskin earthquakes (USGS
539 2019). Contours with an interval of 20 km denote the subducting slab surface in the model of
540 Hayes et al. (2018). The dashed bold line demarks the approximate boundary of the Pacific Plate
541 and the Yakutat terrane, and two arrows show their plate motions relative to the overlying North
542 America Plate. The triangles and dashed ellipse show the active volcanoes (Alaska Volcano
543 Observatory (AVO) 2016) and the Cook Inlet Basin, respectively. The inset shows the
544 cross-sectional view along the linear profile X–Y.

545

546 **Figure 2** Relocated aftershocks (Ruppert et al. 2020) within the three days following the
547 Anchorage mainshock (plotted points).

548 **a** Map view. The large star marks the epicenter of the mainshock. The two small stars mark the
549 epicenters of the aftershocks used for the calibration of the 1D velocity structure models. The
550 dashed and dotted ellipses denote the southern and northern aftershock clusters, respectively. **b**
551 Cross-sectional view of the aftershocks along the linear profile A–B. The bold line indicates the
552 slab surface.

553

554 **Figure 3** Fault planes for the three inversion cases.

555 The upper and lower panels depict the map and cross-sectional views, respectively. The
556 orientation of the cross-sectional views is the same as that in Figure 2b. The bold frames and
557 lines denote the fault planes. The large green star denotes the rupture initiation point (the
558 hypocenter). The small black star denotes the rupture initiation point on segment S3. The bold
559 arrows schematically show the rupture propagation direction on each fault plane. The aftershocks

560 are shown in all panels as the plotted points. The black lines in the lower panels denote the slab
561 surface.

562

563 **Figure 4** 1D *S*-wave velocity structure models.

564 The solid and dashed lines indicate the calibrated and initial velocity structure models,
565 respectively. The map view shows the mainshock epicenter (star) and stations (triangles). The
566 stations marked by solid triangles were used for the inversions. The physical parameters in the
567 calibrated models are shown in Table S2.

568

569 **Figure 5** Final slip for a preliminary inversion trial.

570 **a** Cross-sectional view of the fault plane (bold line). **b** Map view of the final slip. The orientation
571 of the cross-sectional view is the same as that in Figures 2b and 3. The star and plotted points
572 show the rupture initiation point and the aftershocks, respectively.

573

574 **Figure 6** Map views of the final slips for the three inversion cases (A, B, and C).

575 The large yellow star denotes the rupture initiation point (the hypocenter). The small purple star
576 denotes the rupture initiation point on segment S3. The thick solid lines indicate the upper edges
577 of the fault planes. The plotted points show the aftershocks.

578

579 **Figure 7** Planar view of the inversion result for case A.

580 **a** Final slip. **b** Maximum slip velocity and moment rate function. The star denotes the rupture
581 initiation point.

582

583 **Figure 8** Planar view of the inversion result for case B.

584 **a** Final slip. **b** Maximum slip velocity and moment rate function. The stars denote the rupture
585 initiation point on each fault plane. The two rectangles show the large slip areas A1 and A2
586 extracted using the criteria of Somerville et al. (1999).

587

588 **Figure 9** Planar view of the inversion result for case C.

589 **a** Final slip. **b** Maximum slip velocity and moment rate function. The stars denote the rupture
590 initiation points on each fault plane

591

592 **Figure 10** Comparison between the observed and synthetic velocity waveforms (0.05–0.4 Hz)
593 during the mainshock.

594 **a** For each station, the observed waveforms and synthetic waveforms for cases A, B, and C are
595 arranged in order from top to bottom. The amplitudes of each waveform were normalized to the
596 peak amplitudes of the observed three-component waveforms. The number to the right of each
597 waveform denotes the peak amplitude in cm/s. **b** Detailed view of the east–west component of
598 station AHOU. The two arrows indicate the main pulses. The observed waveform, synthetic
599 waveforms calculated by assuming segments S1 and S2 (case A) and segments S1 and S3 (case
600 B), and synthetic waveforms calculated by assuming only segment S2 (case A) and segment S3
601 (case B) are arranged in order from top to bottom.

602

603 **Figure 11** Comparison of the synthetic velocity waveforms (east–west component; 0.05–0.4 Hz)
604 for two virtual line source models with the observed velocity waveforms.

605 The number to the right of each waveform denotes the peak amplitude in cm/s. The map view

606 shows the hypocenter (stars), segments S2 and S3 (gray rectangles), stations (triangles), line
607 sources (bold lines), and rupture propagation direction on each line fault (arrows).

608

609 **Figure 12** Detailed source rupture propagation for case B.

610 **a** Snapshots of the source rupture propagation. The stars in the upper panels denote the first
611 rupture initiation point (the hypocenter). The stars in the lower panels denote the second rupture
612 initiation point on segment S3. The two rectangles show the large slip areas A1 and A2. **b**
613 Velocity waveforms (0.05–0.4 Hz) in the east–west component at the three near-source stations.
614 For each station, the first waveforms from the top show a comparison between the observation
615 and the synthetic calculated for the entire fault. The second and third waveforms from the top
616 show the synthetics calculated using only the large slip areas A1 and A2, respectively. The map
617 view shows the location of the stations (triangles), the epicenter (star), and the large slip areas
618 (rectangles).

619

620 **Figure 13** Source scaling relationships of intraslab earthquakes.

621 **a** Dimension of the large slip areas. **b** Dimension of the rupture area. **c** Average slip of the
622 rupture area. The dashed lines show the standard deviations of the scaling relationships (solid
623 lines). Note that Allen and Hayes (2017) did not include a relationship for the dimension of the
624 large slip areas.

625

626 **Figure 14** Velocity Fourier spectra (east–west component) at the stations in downtown
627 Anchorage during the mainshock.

628 The map view shows the location of the stations (triangles) and the epicenter (star).

Figures

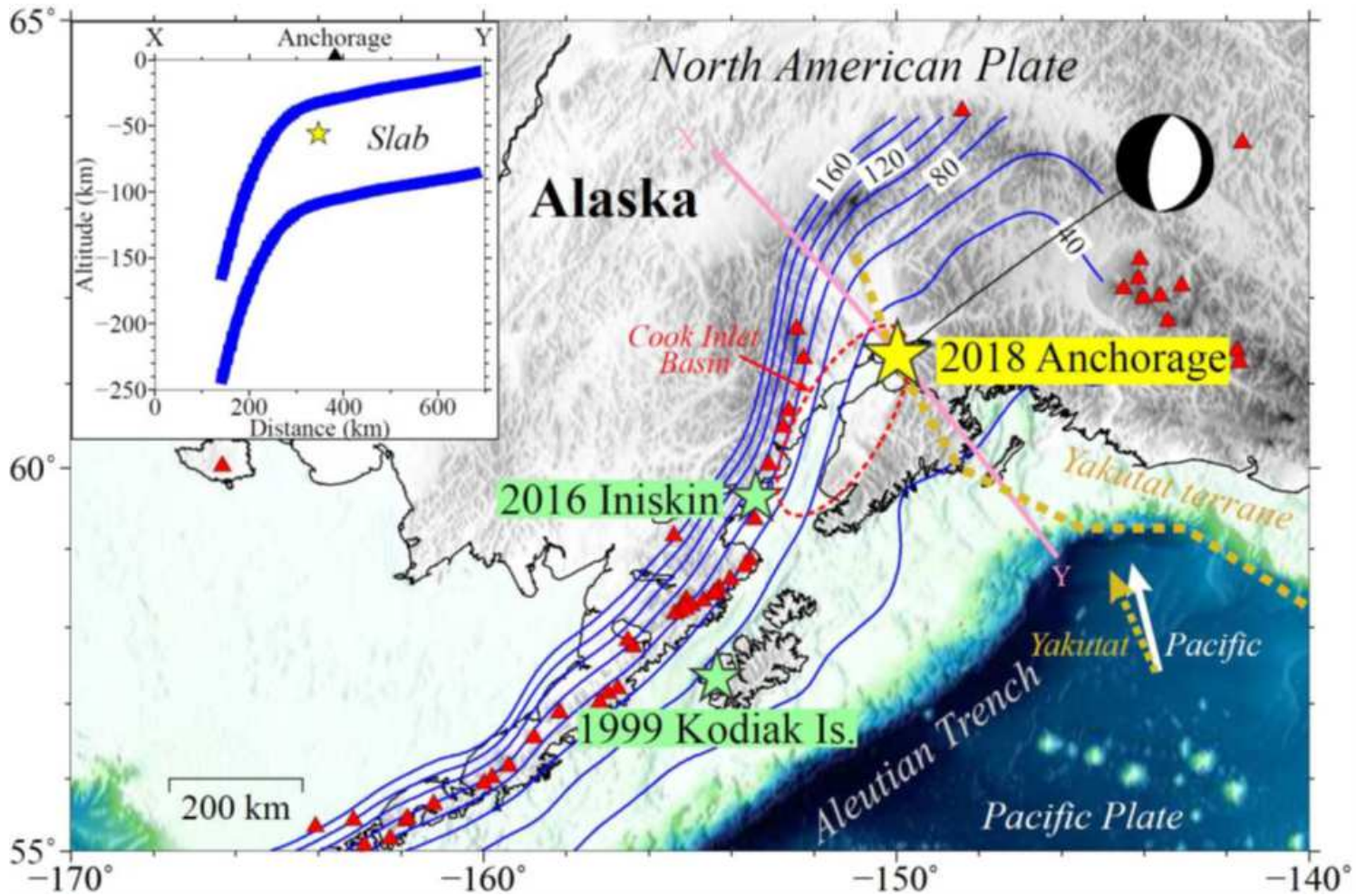


Figure 1

Map of southern Alaska. Stars mark the epicenters of the Anchorage, Kodiak Island, and Iniskin earthquakes (USGS 2019). Contours with an interval of 20 km denote the subducting slab surface in the model of Hayes et al. (2018). The dashed bold line demarks the approximate boundary of the Pacific Plate and the Yakutat terrane, and two arrows show their plate motions relative to the overlying North America Plate. The triangles and dashed ellipse show the active volcanoes (Alaska Volcano Observatory (AVO) 2016) and the Cook Inlet Basin, respectively. The inset shows the cross-sectional view along the linear profile X-Y.

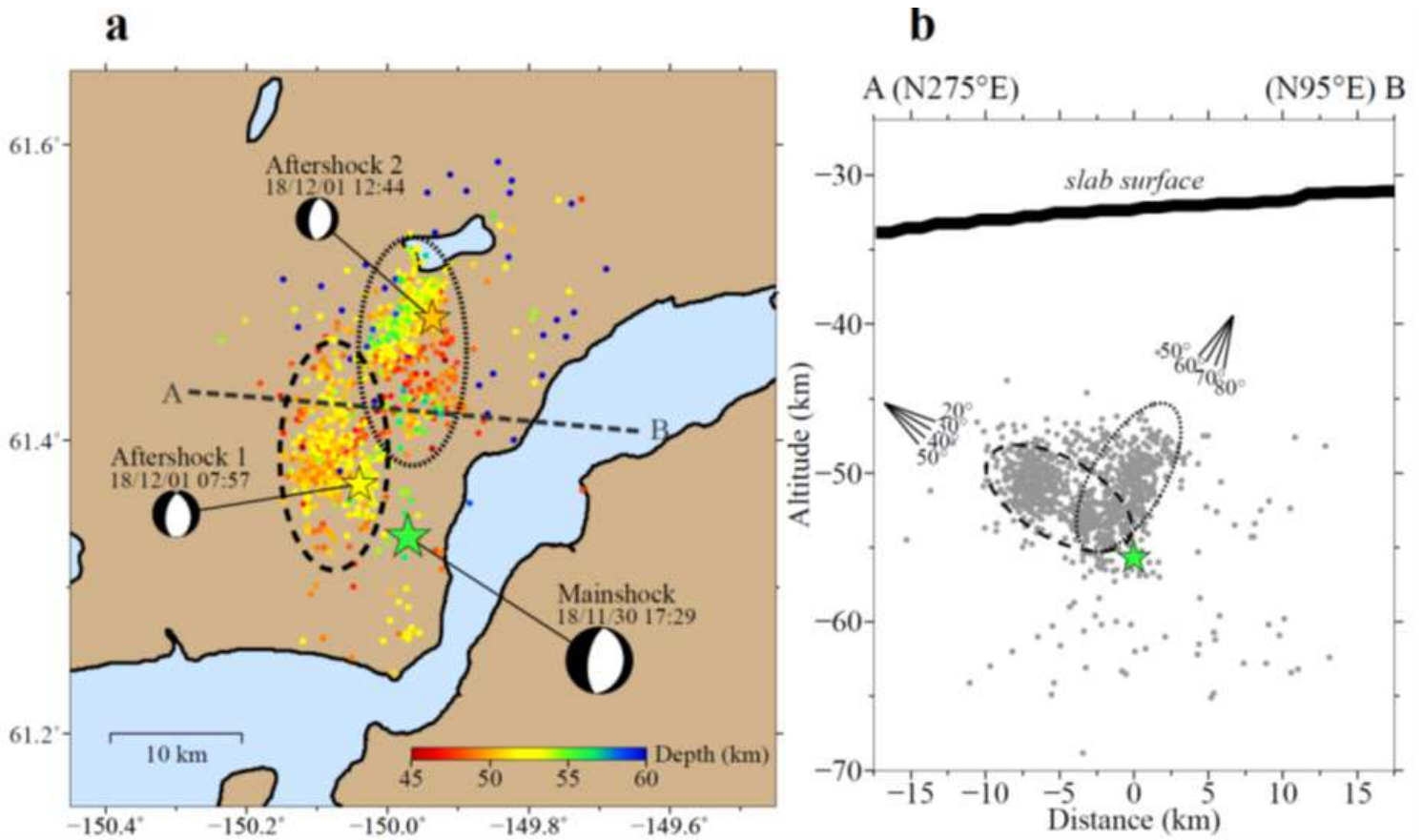


Figure 2

Relocated aftershocks (Ruppert et al. 2020) within the three days following the Anchorage mainshock (plotted points). a Map view. The large star marks the epicenter of the mainshock. The two small stars mark the epicenters of the aftershocks used for the calibration of the 1D velocity structure models. The dashed and dotted ellipses denote the southern and northern aftershock clusters, respectively. b Cross-sectional view of the aftershocks along the linear profile A–B. The bold line indicates the slab surface.

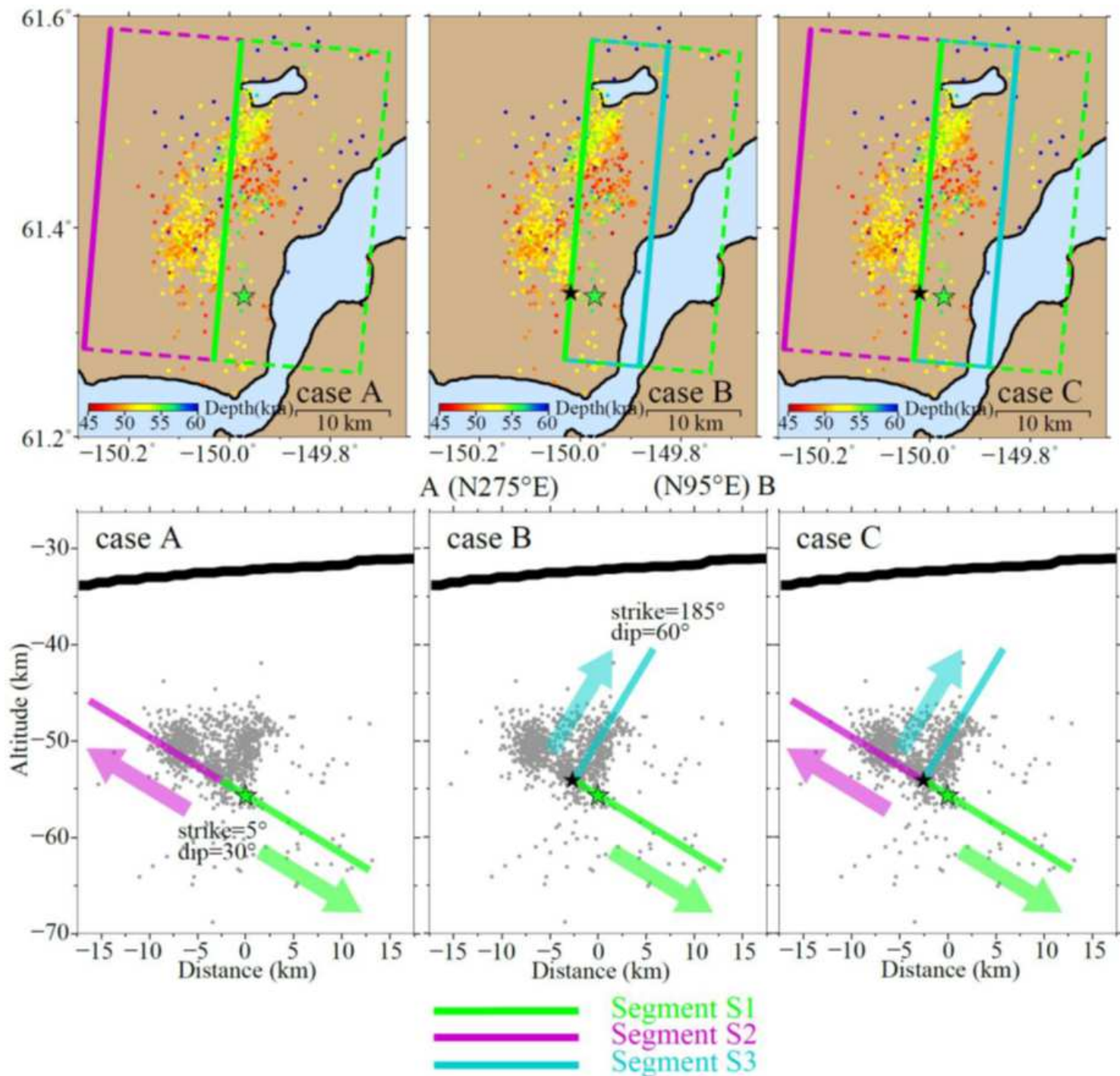


Figure 3

Fault planes for the three inversion cases. The upper and lower panels depict the map and cross-sectional views, respectively. The orientation of the cross-sectional views is the same as that in Figure 2b. The bold frames and lines denote the fault planes. The large green star denotes the rupture initiation point (the hypocenter). The small black star denotes the rupture initiation point on segment S3. The bold arrows schematically show the rupture propagation direction on each fault plane. The aftershocks are shown in all panels as the plotted points. The black lines in the lower panels denote the slab surface.

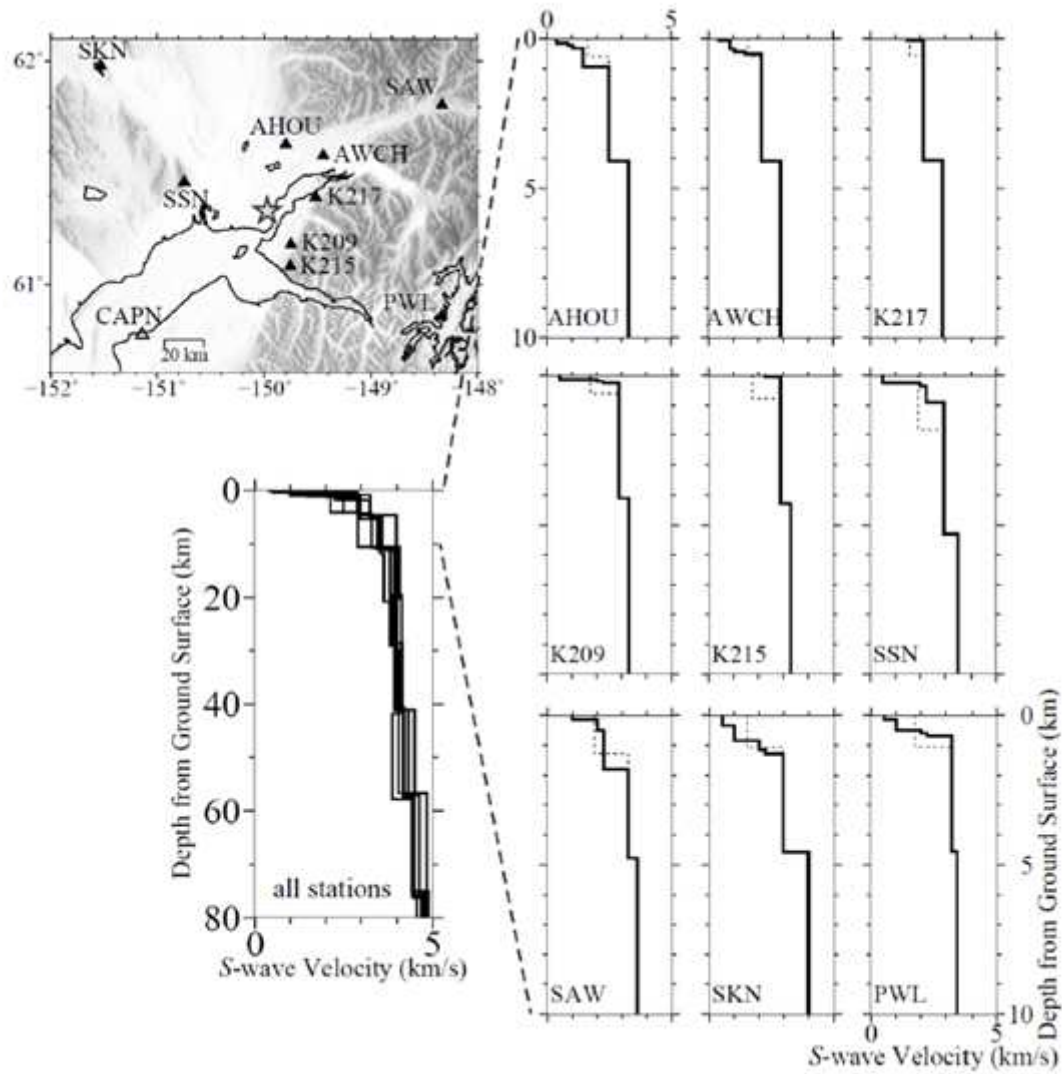


Figure 4

1D S-wave velocity structure models. The solid and dashed lines indicate the calibrated and initial velocity structure models, respectively. The map view shows the mainshock epicenter (star) and stations (triangles). The stations marked by solid triangles were used for the inversions. The physical parameters in the calibrated models are shown in Table S2.

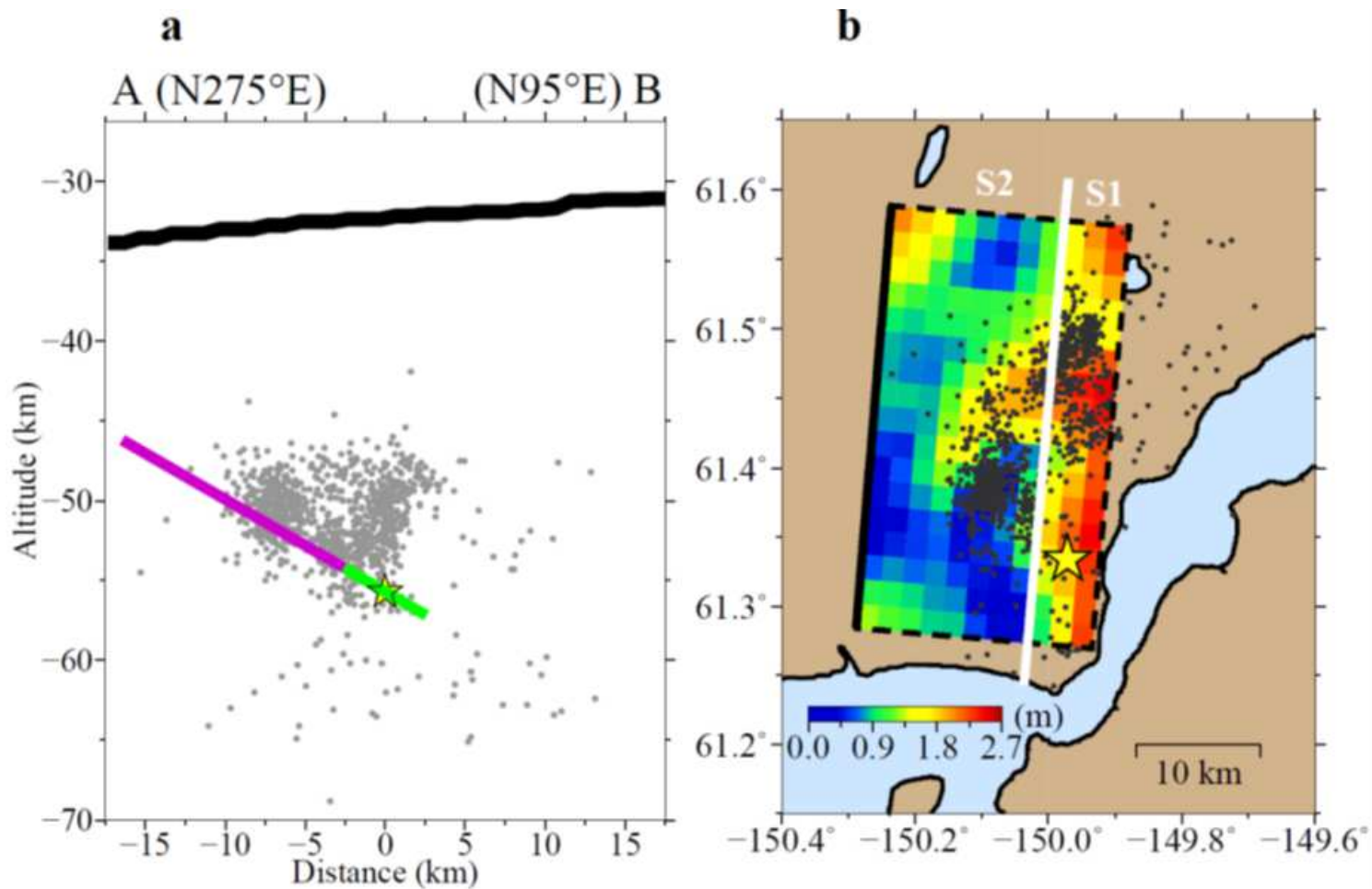


Figure 5

Final slip for a preliminary inversion trial. a Cross-sectional view of the fault plane (bold line). b Map view of the final slip. The orientation of the cross-sectional view is the same as that in Figures 2b and 3. The star and plotted points show the rupture initiation point and the aftershocks, respectively.

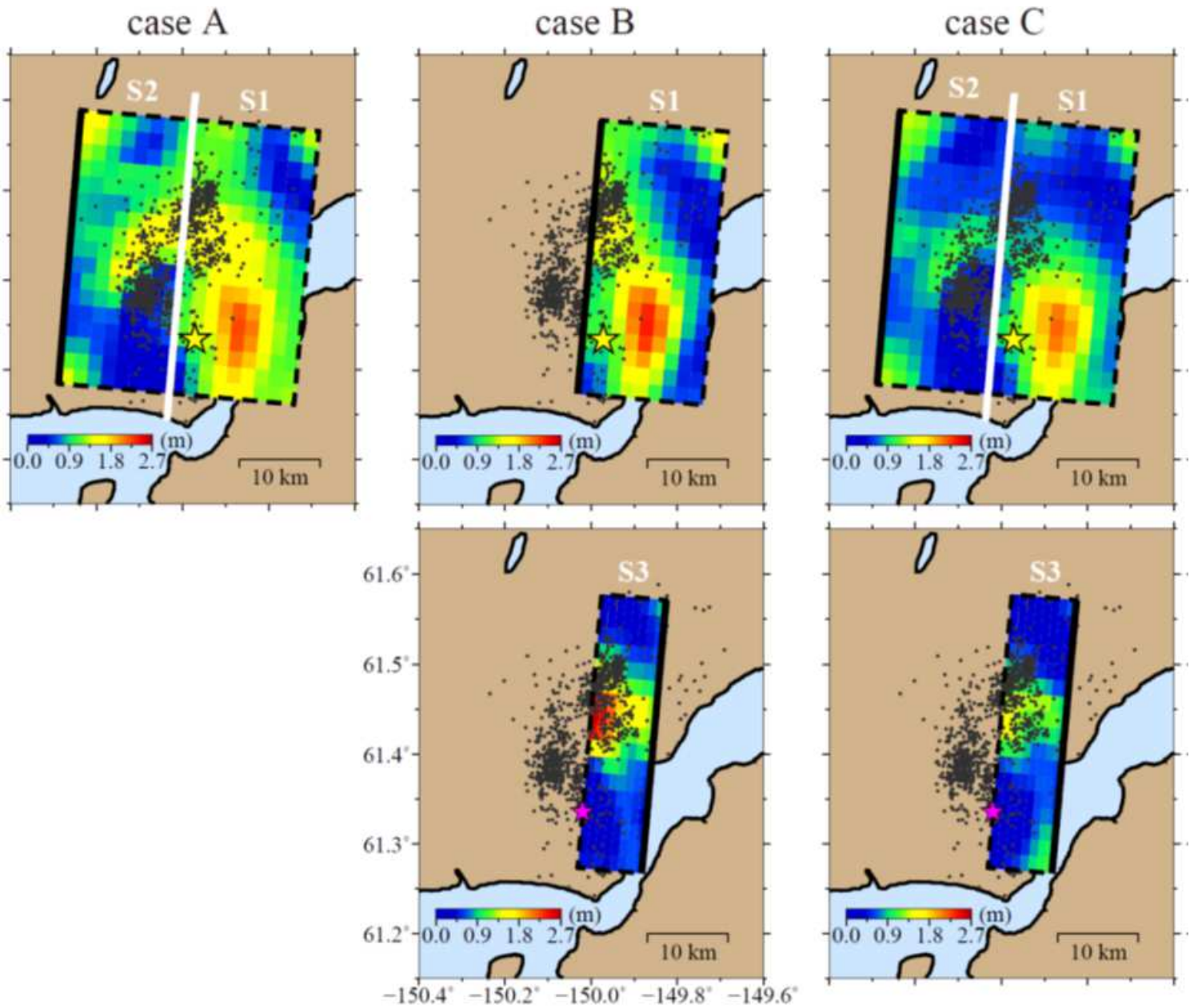


Figure 6

Map views of the final slips for the three inversion cases (A, B, and C). The large yellow star denotes the rupture initiation point (the hypocenter). The small purple star denotes the rupture initiation point on segment S3. The thick solid lines indicate the upper edges of the fault planes. The plotted points show the aftershocks.

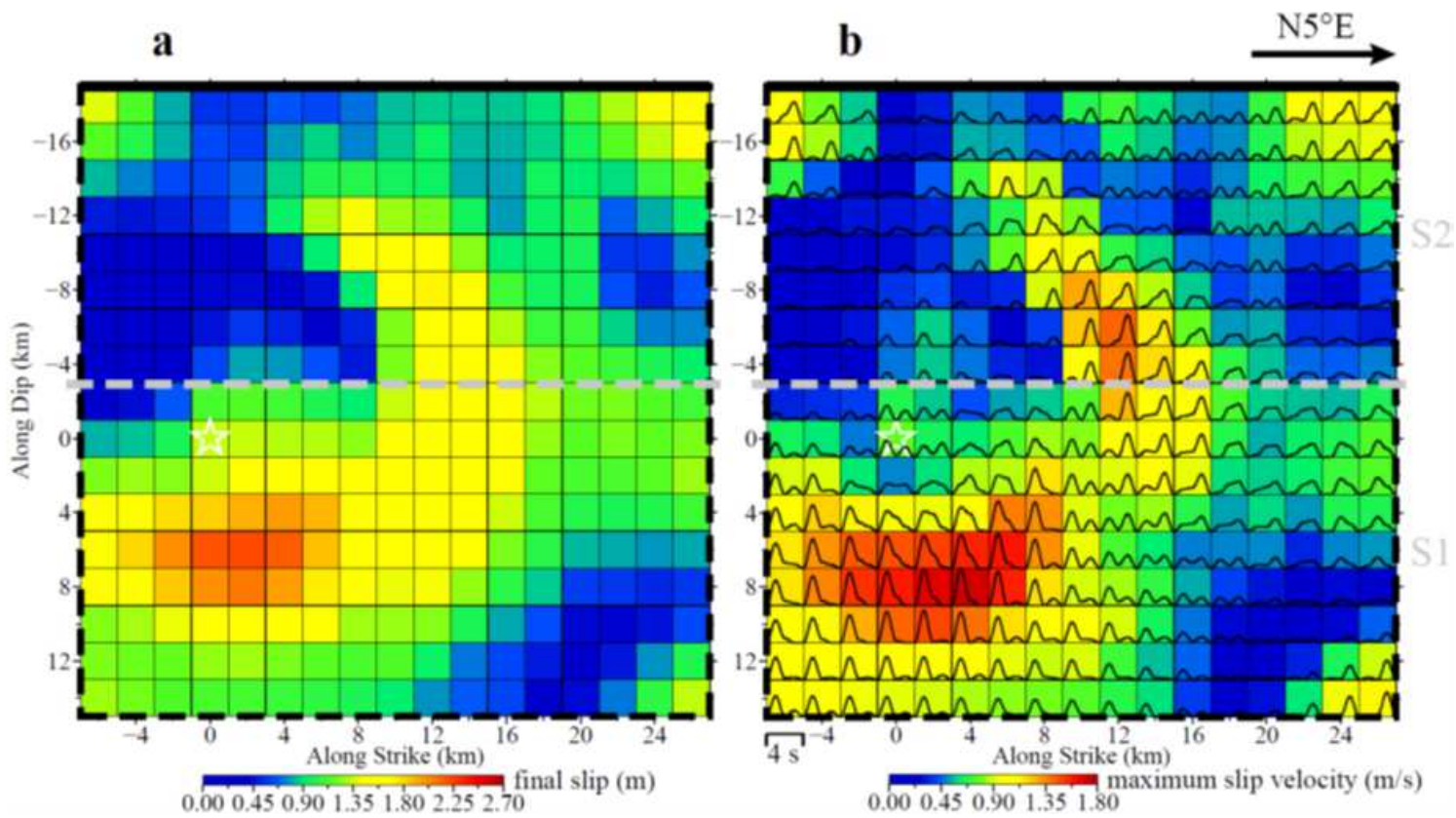


Figure 7

Planar view of the inversion result for case A. a Final slip. b Maximum slip velocity and moment rate function. The star denotes the rupture initiation point.

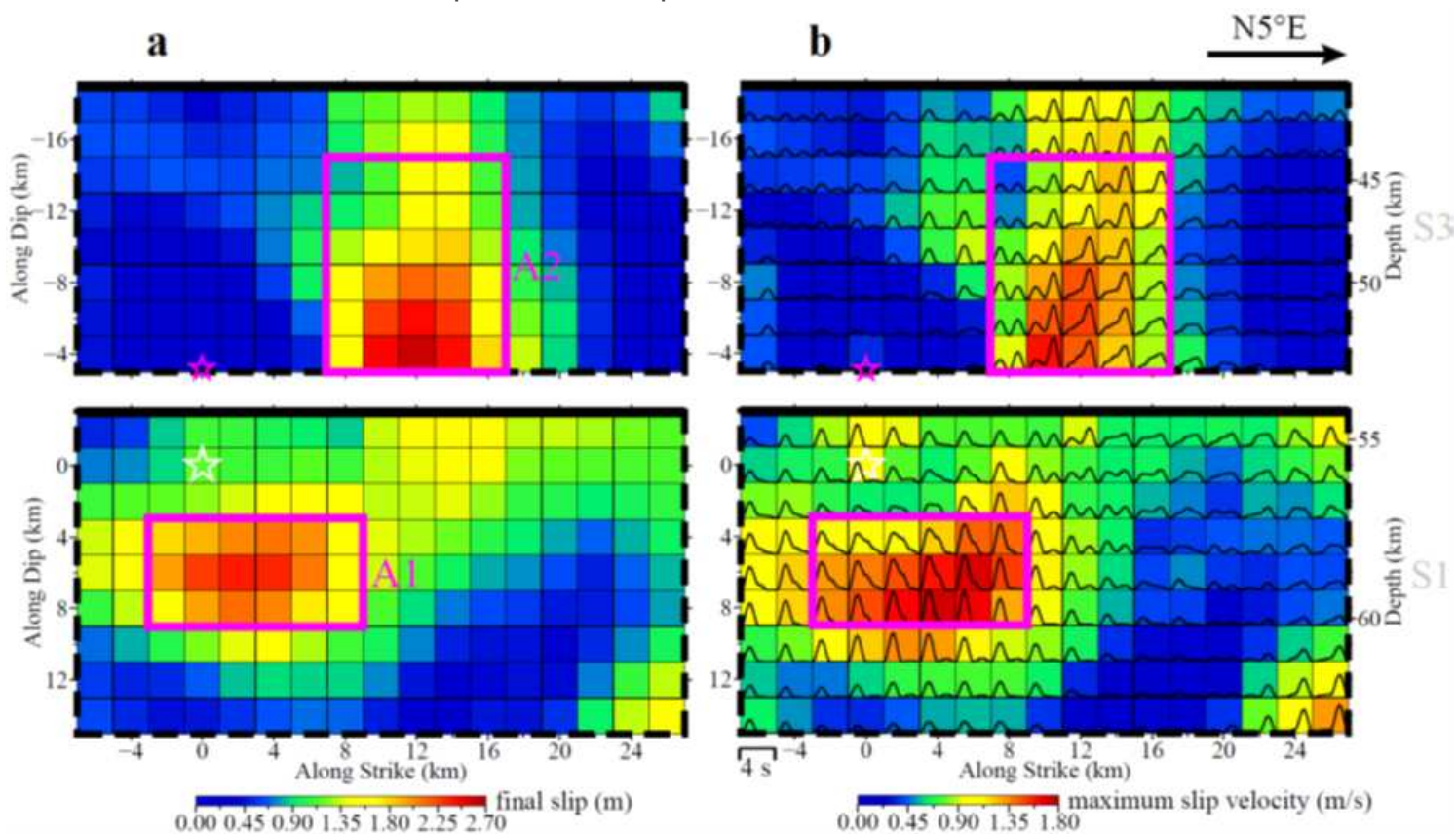


Figure 8

Planar view of the inversion result for case B. a Final slip. b Maximum slip velocity and moment rate function. The stars denote the rupture initiation point on each fault plane. The two rectangles show the large slip areas A1 and A2 extracted using the criteria of Somerville et al. (1999).

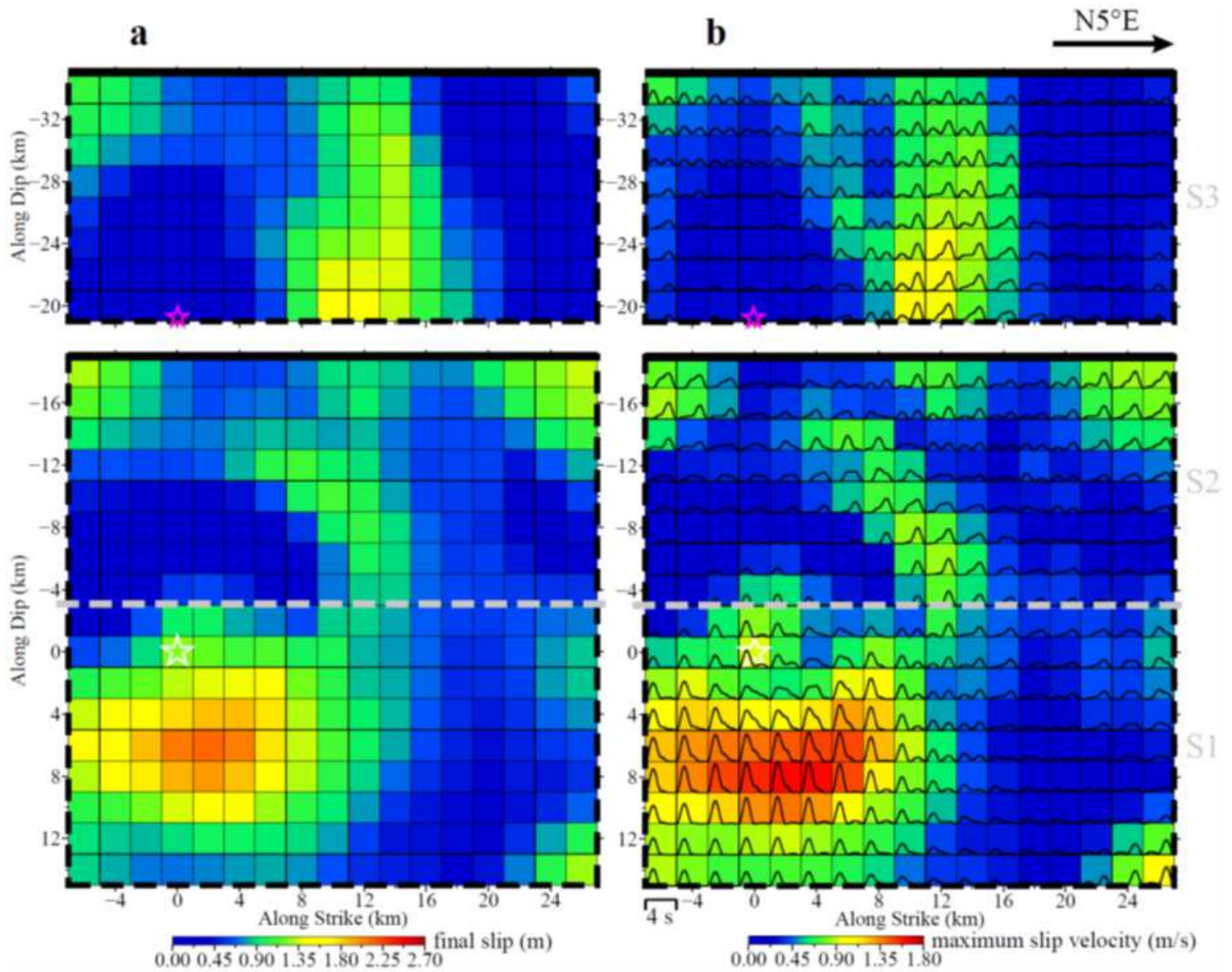


Figure 9

Planar view of the inversion result for case C. a Final slip. b Maximum slip velocity and moment rate function. The stars denote the rupture initiation points on each fault plane

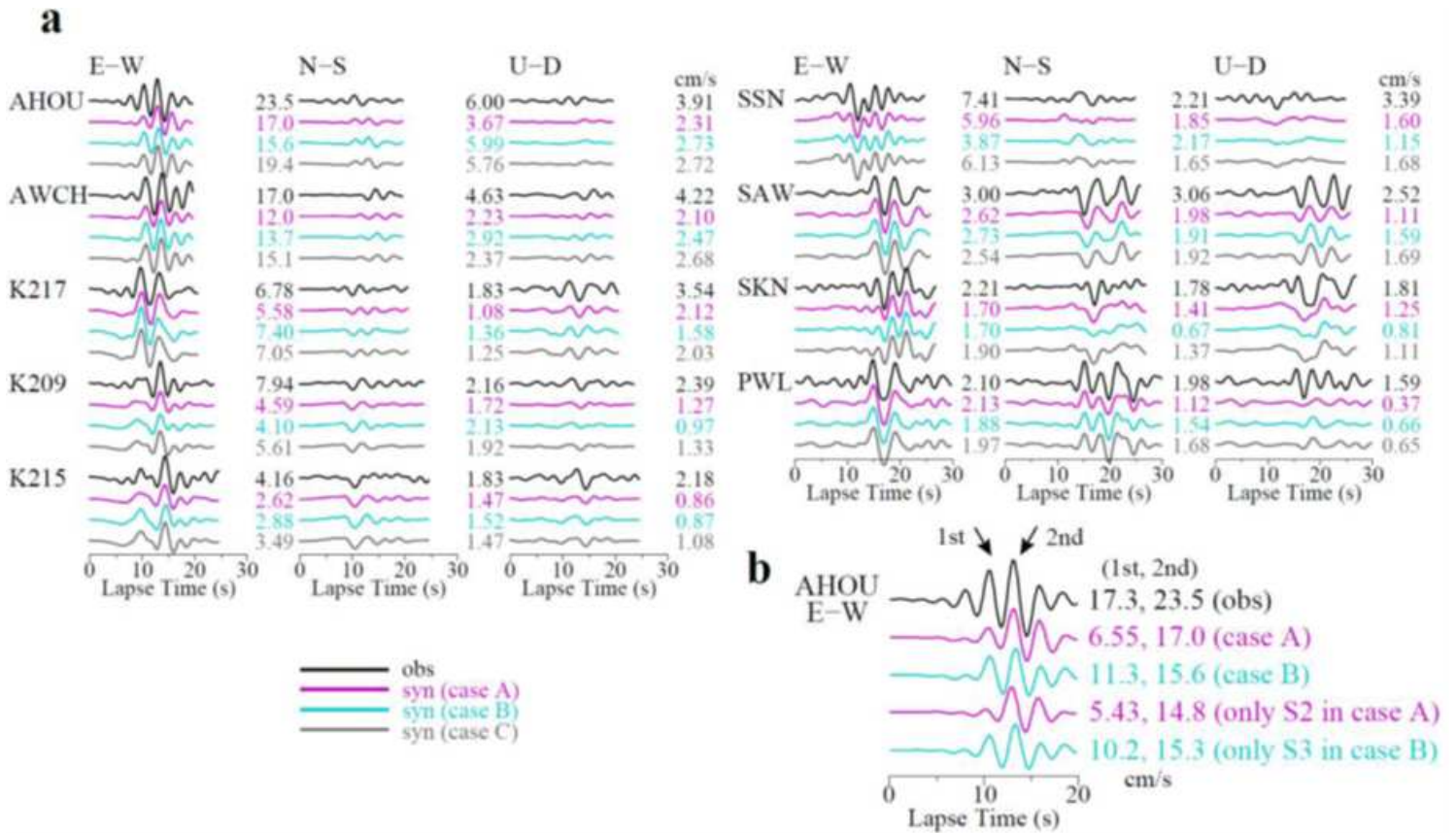


Figure 10

Comparison between the observed and synthetic velocity waveforms (0.05–0.4 Hz) during the mainshock. **a** For each station, the observed waveforms and synthetic waveforms for cases A, B, and C are arranged in order from top to bottom. The amplitudes of each waveform were normalized to the peak amplitudes of the observed three-component waveforms. The number to the right of each waveform denotes the peak amplitude in cm/s. **b** Detailed view of the east–west component of station AHOU. The two arrows indicate the main pulses. The observed waveform, synthetic waveforms calculated by assuming segments S1 and S2 (case A) and segments S1 and S3 (case B), and synthetic waveforms calculated by assuming only segment S2 (case A) and segment S3 (case B) are arranged in order from top to bottom.

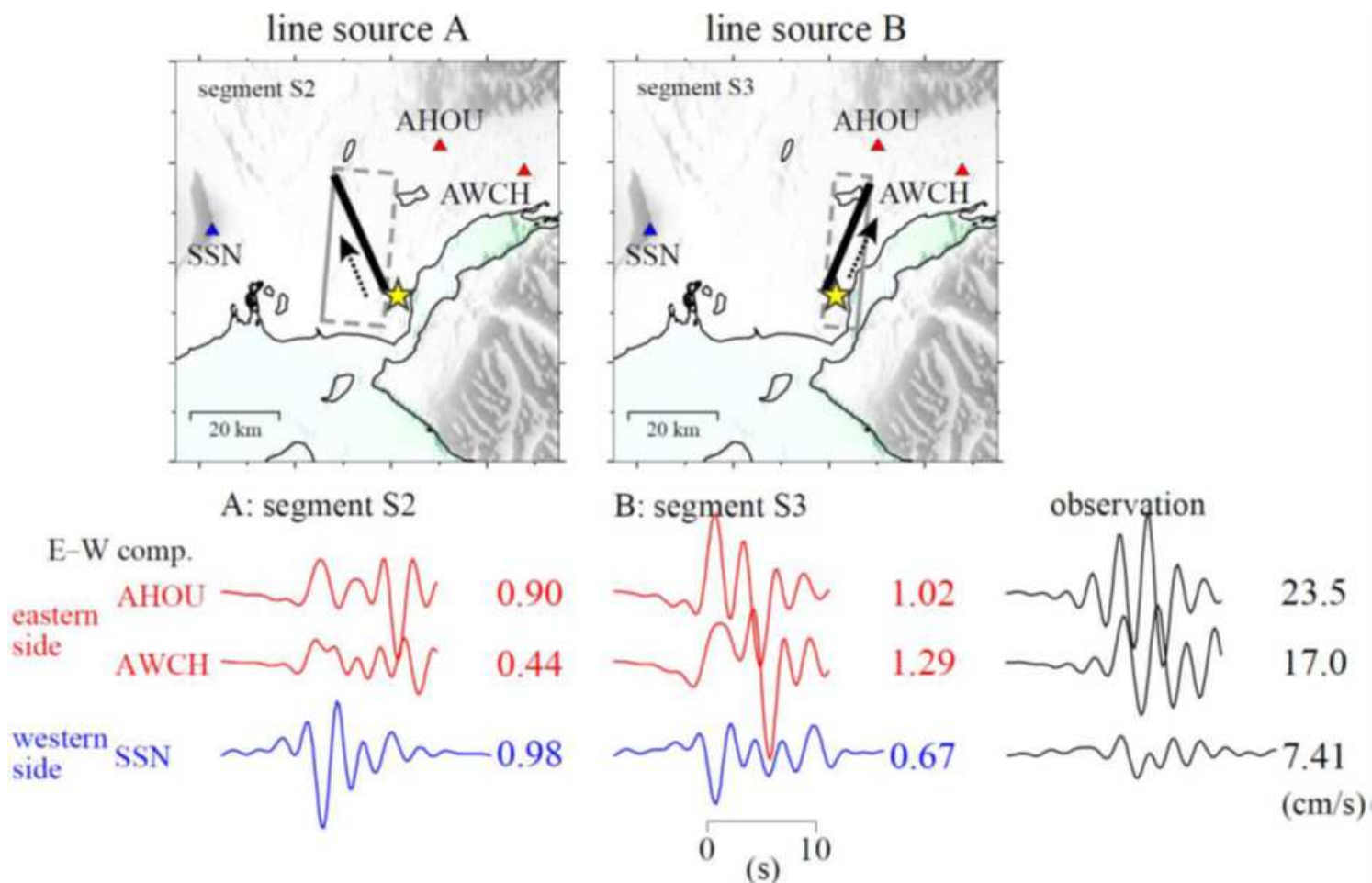


Figure 11

Comparison of the synthetic velocity waveforms (east–west component; 0.05–0.4 Hz) for two virtual line source models with the observed velocity waveforms. The number to the right of each waveform denotes the peak amplitude in cm/s. The map view shows the hypocenter (stars), segments S2 and S3 (gray rectangles), stations (triangles), line sources (bold lines), and rupture propagation direction on each line fault (arrows).

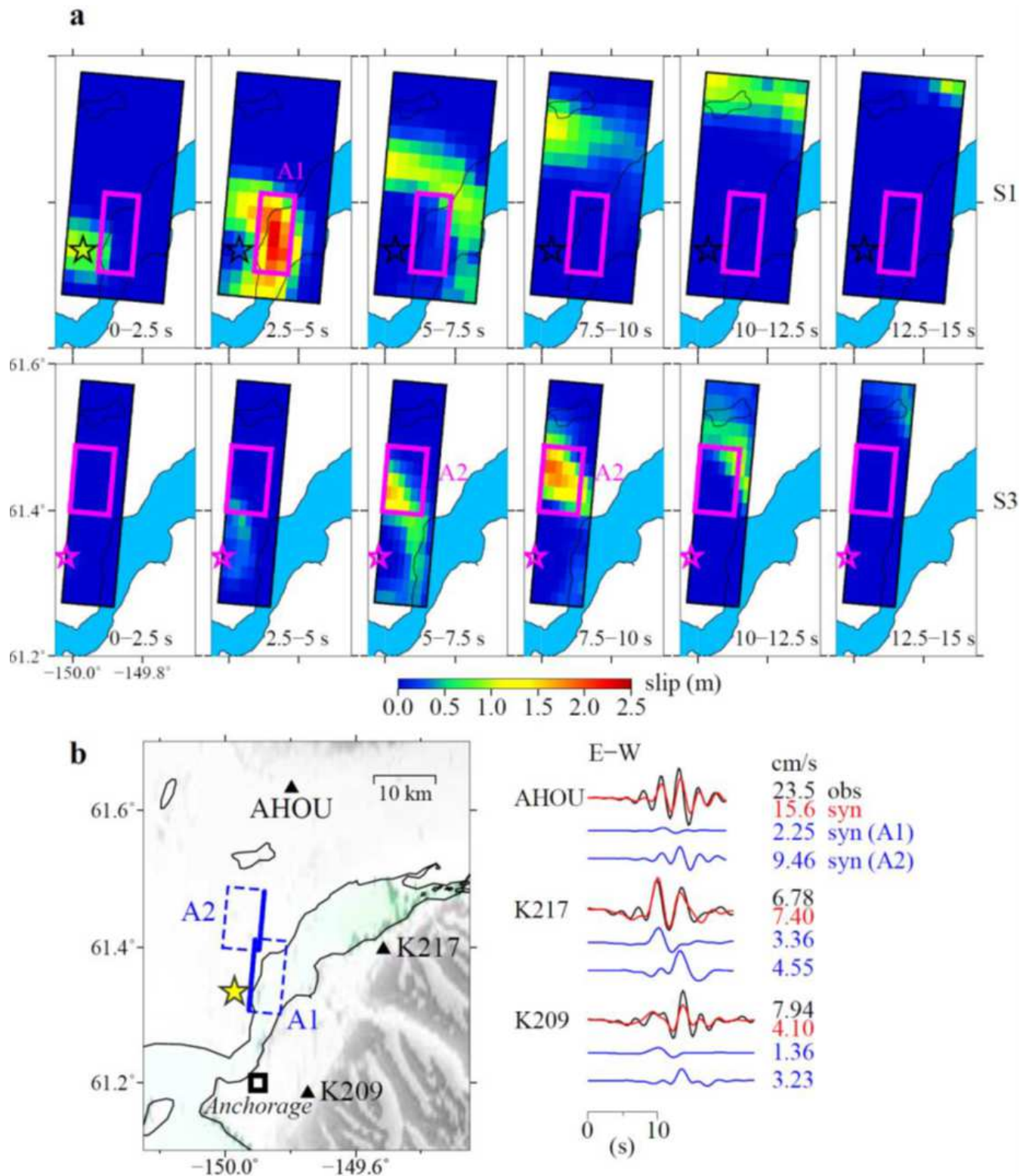


Figure 12

Detailed source rupture propagation for case B. a Snapshots of the source rupture propagation. The stars in the upper panels denote the first rupture initiation point (the hypocenter). The stars in the lower panels denote the second rupture initiation point on segment S3. The two rectangles show the large slip areas A1 and A2. b Velocity waveforms (0.05–0.4 Hz) in the east–west component at the three near-source stations. For each station, the first waveforms from the top show a comparison between the observation

and the synthetic calculated for the entire fault. The second and third waveforms from the top show the synthetics calculated using only the large slip areas A1 and A2, respectively. The map view shows the location of the stations (triangles), the epicenter (star), and the large slip areas (rectangles).

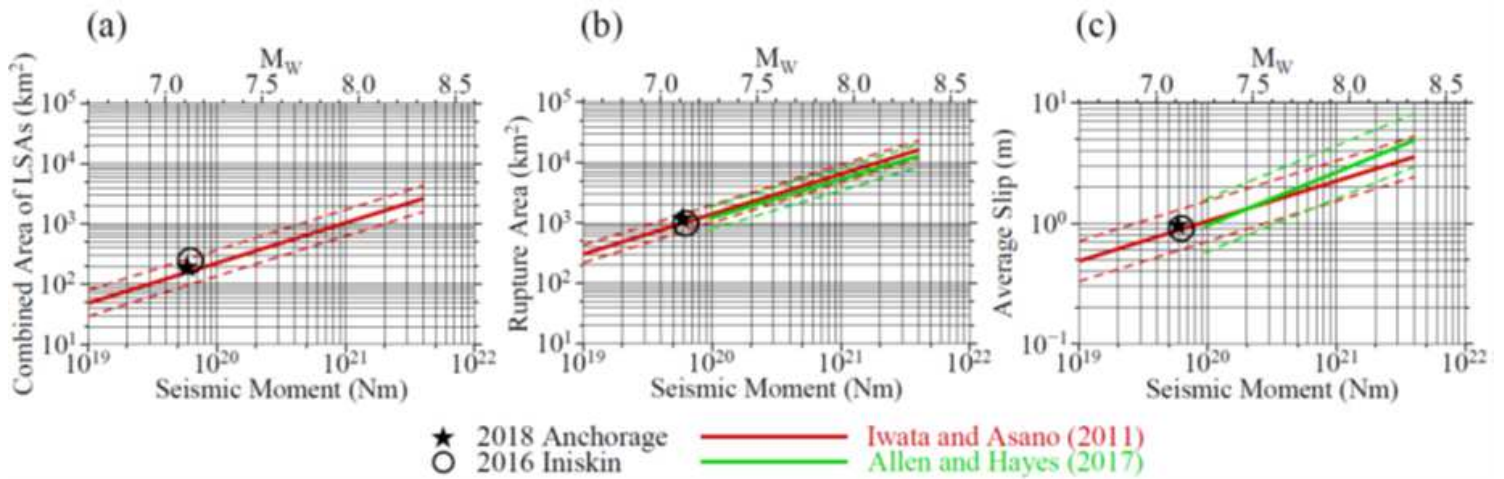


Figure 13

Source scaling relationships of intraslab earthquakes. a Dimension of the large slip areas. b Dimension of the rupture area. c Average slip of the rupture area. The dashed lines show the standard deviations of the scaling relationships (solid lines). Note that Allen and Hayes (2017) did not include a relationship for the dimension of the large slip areas.

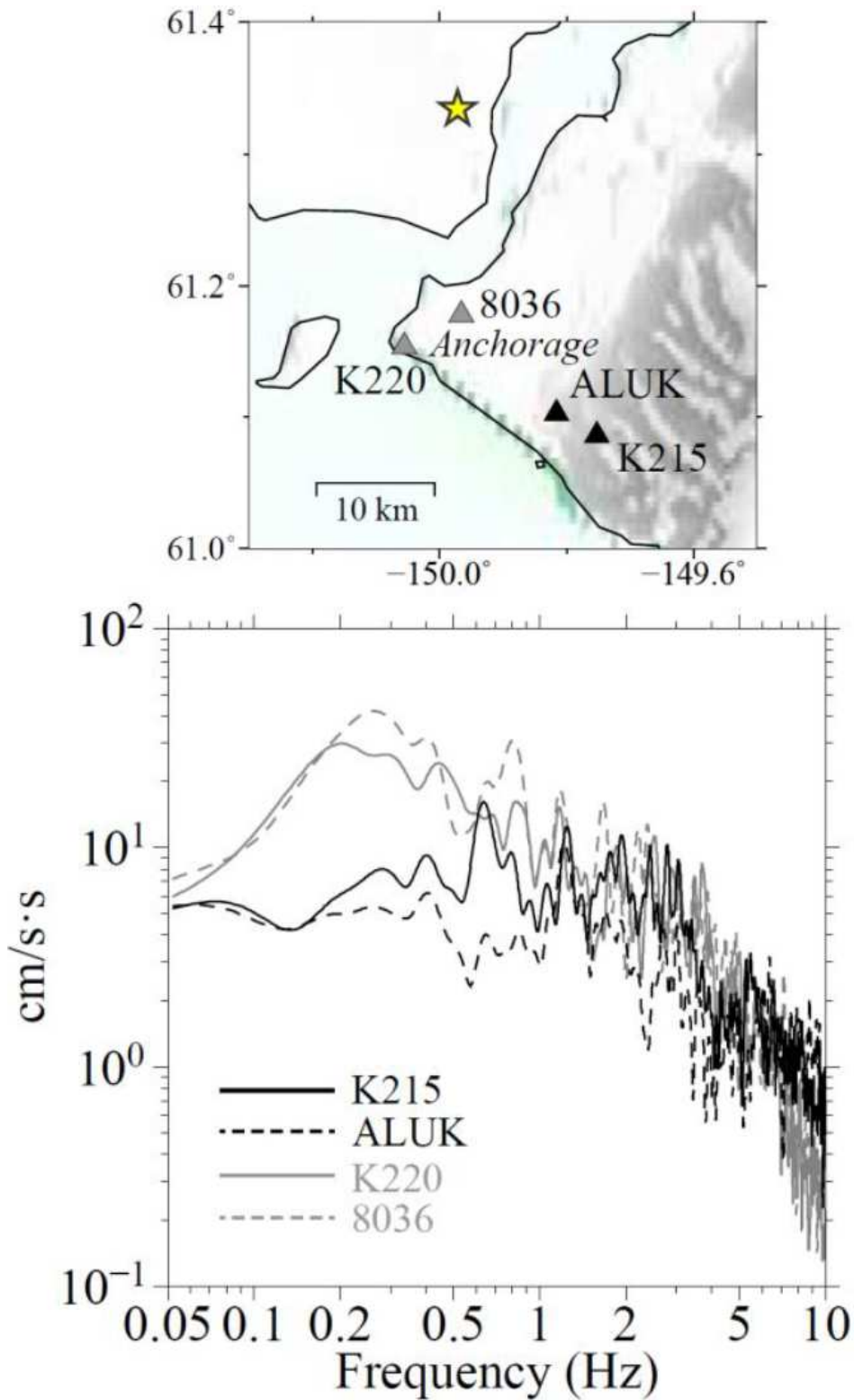


Figure 14

Velocity Fourier spectra (east-west component) at the stations in downtown Anchorage during the mainshock. The map view shows the location of the stations (triangles) and the epicenter (star).

Supplementary Files

This is a list of supplementary files associated with this preprint. Click to download.

- [GuoAnchoEpsGraphicAbst42.png](#)
- [GuoGRIAnchoEpsSpl42.pdf](#)